CLIMATOLOGY

South American monsoon intensification during the last millennium driven by joint Pacific and Atlantic forcing

Zhiqiang Lyu[1]*, Mathias Vuille[1]*, Hugues Goosse[2], Rebecca Orrison[1], Valdir F. Novello[3], Francisco W. Cruz[4], Nicolás M. Stríkis[4,5], Julio Cauhy[6]

The South American summer monsoon (SASM) profoundly influences tropical South America's climate, yet understanding its low-frequency variability has been challenging. Climate models and oxygen isotope data have been used to examine the SASM variability over the last millennium (LM) but have, at times, provided conflicting findings, especially regarding its mean-state change from the Medieval Climate Anomaly to the Little Ice Age. Here, we use a paleoclimate data assimilation (DA) method, combining model results and $\delta^{18}O$ observations, to produce a $\delta^{18}O$-enabled, dynamically coherent, and spatiotemporally complete austral summer hydroclimate reconstruction over the LM for tropical South America at 5-year resolution. This reconstruction aligns with independent hydroclimate and $\delta^{18}O$ records withheld from the DA, revealing a centennial-scale SASM intensification during the MCA-LIA transition period, associated with the southward shift of the Atlantic Intertropical Convergence Zone and the strengthening Pacific Walker circulation (PWC). This highlights the necessity of accurately representing the PWC in climate models to predict future SASM changes.

INTRODUCTION

The South American summer monsoon (SASM) is a major southern hemisphere monsoon system that is active during December, January, and February (DJF) and accounts for up to 70% of the annual precipitation over large parts of tropical and subtropical South America (*1*–*3*). Despite decades of research enhancing our understanding of the SASM dynamics on interannual and decadal timescales (*1*, *3*), its behavior over longer timescales is less understood, primarily due to the scarcity and short length of instrumental data. Previous research has found that the observed isotopic composition of precipitation ($\delta^{18}O$) over the SASM region can trace the local hydroclimate and the regional atmospheric circulation (*4*–*6*). Consequently, the development of many precisely dated, high-resolution oxygen isotope records spanning the last millennium (LM) has provided important advances in our understanding of past SASM changes, e.g., (*7*–*13*).

A key characteristic of most $\delta^{18}O$ records in tropical South America is the shift in the mean state of $\delta^{18}O$ toward substantially more negative values during the Little Ice Age (LIA; 1450 to 1849 CE) compared to the Medieval Climate Anomaly (MCA; 950 to 1250 CE), particularly within the western and southern portions of the SASM domain (*11*–*13*). Rayleigh distillation theory postulates that isotopic fractionation processes during convective rainout lead to progressively more negative $\delta^{18}O$ in precipitation along moisture trajectories from the Atlantic origin to the ultimate condensation site over the continental interior of tropical South America (*4*, *5*). On the basis of this theory, previous studies proposed two hypotheses to explain the changes in isotopic composition of precipitation during the transition from the MCA to the LIA: (i) Enhanced convective activity associated with a more intense monsoon over its core region, the Amazon basin, resulted in a more negative isotopic composition of precipitation downstream over the western Amazon basin, the tropical Andes and over southeastern South America during the LIA (*11*–*13*); and (ii) increased rainfall over the Atlantic Intertropical Convergence Zone (ITCZ) resulted in a more negative isotopic composition of precipitation downstream over tropical South America, without markedly changing the local rainfall amounts in the SASM region (*14*). To date, neither hypothesis has been validated, as the state-of-the-art climate models fail to fully replicate the hydroclimatic changes that occurred during the transition from the MCA to the LIA as indicated by $\delta^{18}O$ and hydroclimate paleo-records (fig. S1) (*12*, *15*, *16*).

The existing discrepancy between modeling results and proxy records complicates our understanding of the continental-scale $\delta^{18}O$ changes over the LM. This raises several critical questions: Is there a specific continental-scale hydroclimate response pattern that explains the signal observed in the proxy records? If so, is this pattern the result of a strengthened monsoon or rather caused by the southward shift and intensification of the ITCZ over the Atlantic? Furthermore, what is the mechanism underlying these centennial-scale variations in the SASM that would lead to such a marked and persistent transition from the MCA to the LIA? To address these questions, we present a hydroclimate reconstruction over tropical South America spanning the LM, using offline data assimilation (DA) based on a particle filter. This method enables merging oxygen isotope proxy records over the American Neotropics (encompassing the tropical Americas across both hemispheres, as detailed in Fig. 1A and table S1) with the full-field dynamical constraints provided by the isotope-enabled Community Earth System Model (iCESM1) (*17*). We choose iCESM1 simulations given their capacity to provide sufficient particles, preventing particle filter degeneracy (fig. S2) (*18*). Consequently, our DA reconstruction provides a $\delta^{18}O$-enabled, dynamically coherent, and spatiotemporally complete hydroclimate reconstruction over the LM in tropical South America. It allows investigating the spatiotemporal characteristics

[1]Department of Atmospheric and Environmental Sciences, University at Albany, State University of New York, Albany, NY, USA. [2]Earth and Life Institute, Université Catholique de Louvain, Louvain-la-Neuve, Belgium. [3]Department of Geosciences, University of Tübingen, Tübingen, Germany. [4]Geosciences Institute, University of Sao Paulo, Sao Paulo, Brazil. [5]Department of Geochemistry, Federal Fluminense University, Niterói, Brazil. [6]Institute for Geosciences, Johannes Gutenberg University Mainz, Mainz, Germany.
*Corresponding author. Email: mvuille@albany.edu (M.V.); zlyu2@albany.edu (Z.L.)

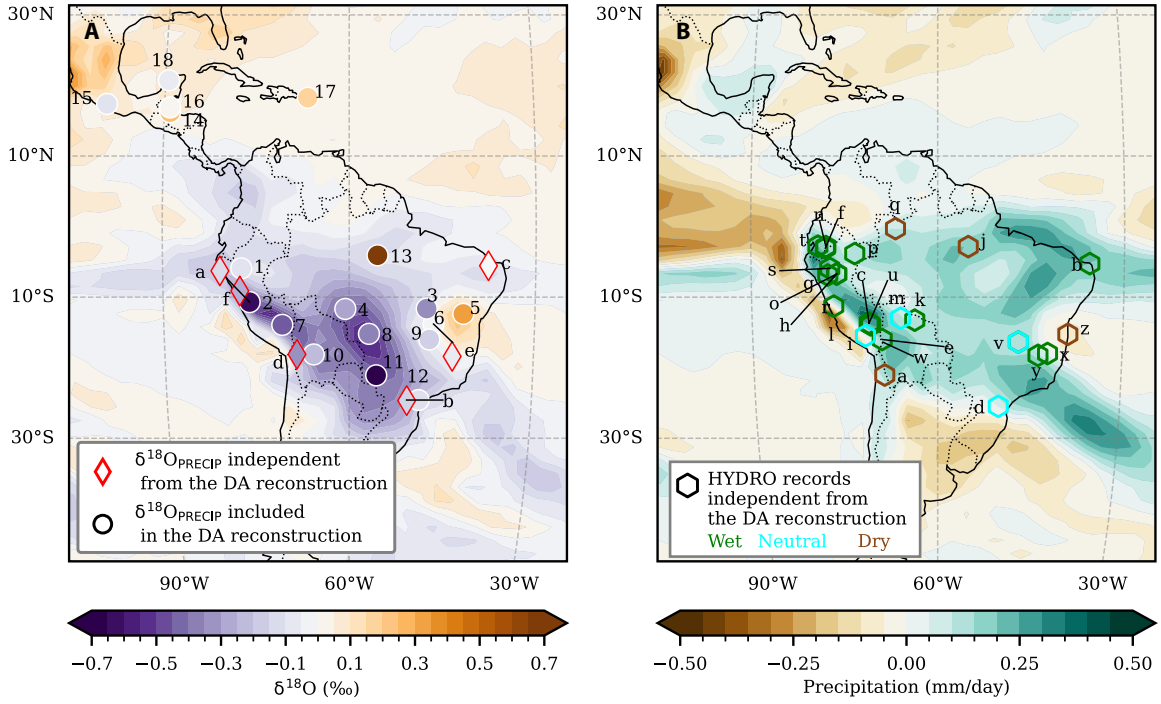

Fig. 1. Validation of the DA reconstruction of mean-state change of $\delta^{18}O$ and DJF precipitation between the LIA and the MCA (LIA-MCA) over tropical South America. The figure indicates the mean values during the LIA (1450 to 1849 CE) minus the mean during the MCA (950 to 1250 CE). The background shading in (**A**) and (**B**) shows the values based on the DA reconstruction. Independent $\delta^{18}O$ records ($\delta^{18}O_{PRECIP}$) that were withheld from the DA are denoted by diamond symbols in (A), while independent local hydroclimate records (HYDRO) are shown as hexagon symbols in (B). Records indicating drier (wetter) conditions during the LIA compared to the MCA are colored brown (green), while records showing no clear changes between the two periods are depicted in cyan in (B).

of the SASM variations during the LM and yields insight into the physical mechanisms responsible for the centennial-scale hydroclimate variability as constrained by the isotopic proxy records.

RESULTS

Validation with $\delta^{18}O$ and precipitation

Given that our DA reconstruction relies on iCESM1 as the prior, it inherently incorporates biases due to the model's limitations (detailed in Materials and Methods and fig. S3, A to I). To evaluate the fidelity of our reconstructed DJF precipitation-weighted $\delta^{18}O$, we use a quantitative statistical approach, integrating independent low-frequency $\delta^{18}O$ records (referred to as $\delta^{18}O_{PRECIP}$, detailed in table S2) over tropical South America. Overall, our reconstruction presents much better agreement with the observed $\delta^{18}O_{PRECIP}$ for the LM (r_{mean} = 0.49; fig. S4, A to F) than the iCESM1 prior (r_{mean} = 0.13) and results in an ~25% reduction of the root mean square error in the reconstruction of the mean-state changes during the transition from the MCA to the LIA when compared to the iCESM1 (fig. S4G).

Moreover, to validate the mean-state change in the reconstructed precipitation from the MCA to the LIA, we conduct a comparative analysis with independent, locally hydroclimate-sensitive reconstructions (denoted "HYDRO" in Fig. 1B and listed in table S3). We find that the majority of HYDRO records (17 of 26; fig. S5) from tropical South America indicate wetter conditions during the LIA compared to the MCA. This characteristic is generally reflected in our DA-reconstructed precipitation during the transition from the MCA to the LIA (Fig. 1B). The agreement between our DA-reconstructed precipitation and the HYDRO data is much better than that between the prior and the data (figs. S1 and S6). It is important, however, to note a geographical bias in these records, as they predominantly originate from the tropical Andean region. Nevertheless, the overall agreement between our reconstruction and these two independent datasets ($\delta^{18}O_{PRECIP}$ and HYDRO) underscores its robustness on centennial timescales.

Hydroclimate footprint of $\delta^{18}O$

To investigate the hydroclimate footprint linked to $\delta^{18}O$ variability over the LM, we decompose the $\delta^{18}O$ and precipitation into spatio-temporal modes of variability using multivariate empirical orthogonal function (MVEOF) analysis (details in Materials and Methods) (*19*, *20*). The primary spatial mode (MVEOF1; Fig. 2, A and B) for both $\delta^{18}O$ and precipitation, which accounts for 49% of the total variance, displays a dipole pattern: Negative $\delta^{18}O$ loadings (positive for precipitation) are prominent across tropical South America, whereas central eastern Brazil exhibits positive $\delta^{18}O$ loadings (negative for precipitation). The first principal component (PC1) shows a pronounced positive trend during the transition from the MCA to the LIA (Fig. 2C). This PC1 correlates strongly with the entirely proxy-based Monte Carlo EOF1 (MCEOF1) based on oxygen isotope records over tropical South America (r = 0.74 at $P < 0.05$) derived from (*12*). This congruence, despite incorporating high-resolution $\delta^{18}O$ data from tropical North America (Fig. 1A), alongside data from tropical South America as noted by Orrison *et al.* (*12*), indicates that our DA-based reconstruction, integrating both

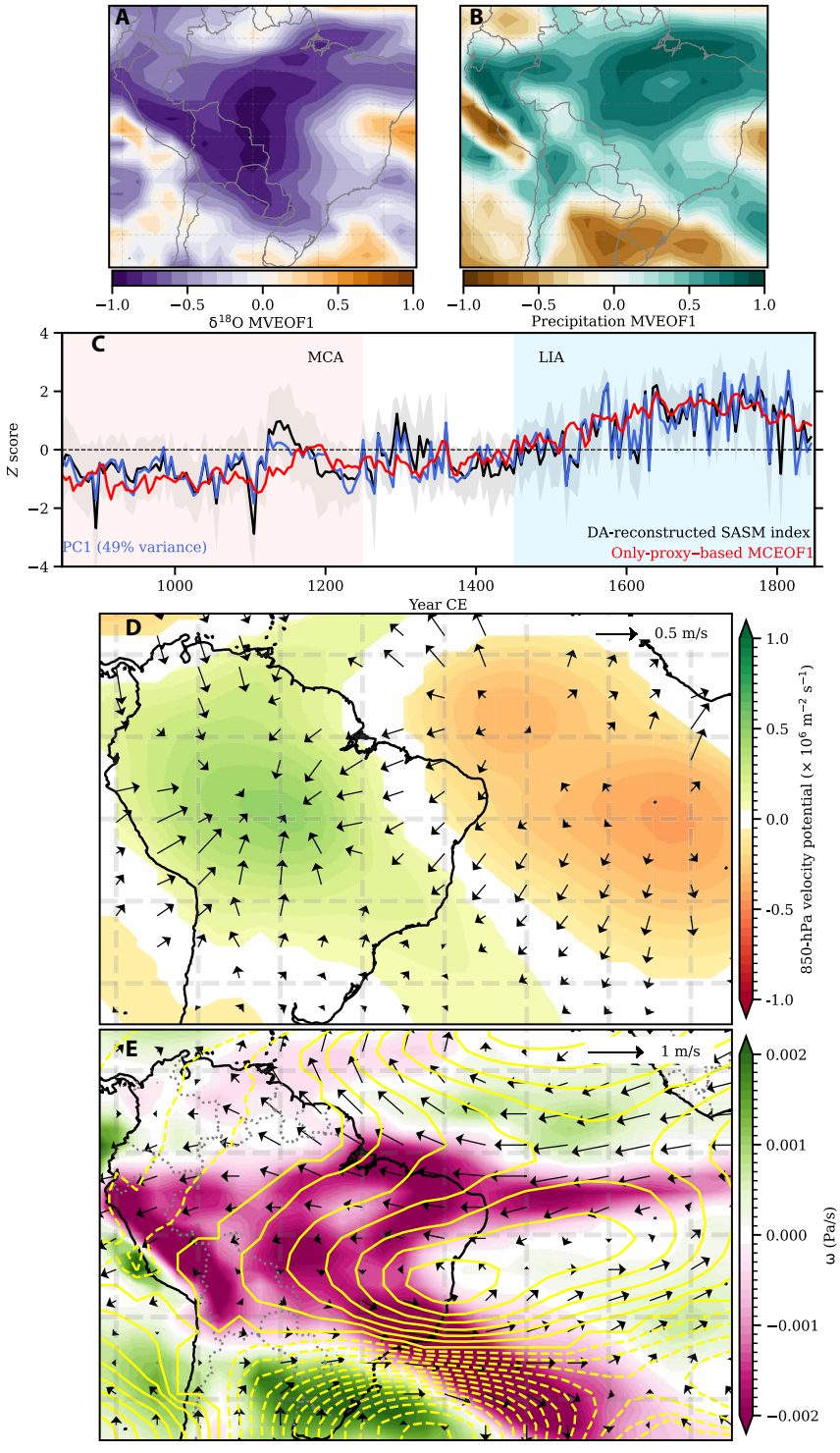

Fig. 2. Leading modes of DJF $\delta^{18}O$ and precipitation over tropical South America, along with the associated atmospheric circulation patterns in the DA reconstruction. (**A** and **B**) Multivariate empirical orthogonal function (MVEOF1) of $\delta^{18}O$ and precipitation over the LM. (**C**) Comparison between the associated principal component (PC) time series (blue), the precipitation-based SASM index (black), and the PC1 from the solely proxy-based Monte Carlo empirical orthogonal function (EOF) analysis derived from (*12*) (red). Shaded areas represent the SD of the ensemble mean from our DA-based reconstruction. All time series are shown with a 5-year temporal resolution. (**D**) Regression of MVEOF PC1 against 850-hPa velocity potential (shading) and divergent wind (vectors). (**E**) Regression of MVEOF PC1 against 500-hPa vertical velocity (ω, shading), 200 hPa wind (vectors) and geopotential height (contours). Contour intervals are 10 geopotential meters, with negative contours dashed. Regression coefficients are plotted only where significant at the 95% confidence level based on a two-tailed Student's *t* test, with degrees of freedom adjusted for the effective sample size to account for serial correlation in the time series.

proxy and model data, accurately captures the dominant spatiotemporal modes of variability mirrored in the proxy records.

The MVEOF1 loading for $\delta^{18}O$ and precipitation over the core monsoon region (2.5°S to 18°S and 45°W to 75°W) indicates a generally negative correlation between them at a continental scale ($r = -0.75$ at $P < 0.05$; fig. S7), aligning with the "amount effect" (*4*, *21*, *22*). However, a closer examination reveals that the highest MVEOF1 loadings for precipitation are notably concentrated over northeastern Brazil, the Amazon Basin, and the tropical Andes. Conversely, the most negative MVEOF1 loadings for $\delta^{18}O$ are predominantly found in the southwestern Amazon basin and over southeastern South America. This spatial offset between precipitation loadings and $\delta^{18}O$ loadings suggests that, consistent with prior research, upstream rainout processes over the Amazon Basin are the principal factor affecting $\delta^{18}O$ in precipitation across the tropical and Central Andes and the Bolivian lowlands (*4*, *6*, *23*, *24*).

To understand the atmospheric dynamics underpinning the MVEOF1 of $\delta^{18}O$ and precipitation during the transition from the MCA to the LIA (Fig. 2C), we regress the PC1 against large-scale atmospheric circulation diagnostics over tropical South America obtained in the DA reconstruction (Fig. 2, D and E). The most visible feature in the low-level circulation is the anomalous convergence at 850 hPa associated with positive loadings of PC1, particularly over the core Amazon area. Given the positive trend of PC1 from MCA toward the LIA (Fig. 2C), this indicates increasing anomalous low-level convergence across the Amazon basin, providing favorable conditions for anomalous ascent and convective activity. The low-level convergence in the Amazon region is coupled with notable upward vertical motion at 500 hPa, with the most pronounced regions of ascent located over the Amazon region and the tropical Andes (Fig. 2E). In addition, a diagonally oriented band of deep convection extends from tropical South America to southeastern Brazil and into the subtropical South Atlantic. This pattern is characteristic of the South Atlantic Convergence Zone (*25*), a region of strong convective activity that is intimately tied to the SASM. In the upper troposphere, there is an anomalous tropical easterly jet and distinct subtropical anticyclonic anomalies straddling the equator, centered at 10° latitude in both hemispheres (Fig. 2E), reflecting the dynamic response to the strengthened convection over the Amazon (*24*). These atmospheric circulation anomalies identified through linear regression–based analysis are consistently observed in the composite analyses as well (figs. S8 and S9), which accounts for complex, nonlinear interactions between the SASM and the corresponding atmospheric circulation. Overall, given the positive trend of the PC1 during the LM (Fig. 2C), these atmospheric configurations indicate a marked intensification of the SASM during the LIA compared to the MCA.

To quantitatively evaluate the fluctuations in SASM intensity, we use precipitation and wind shear–based SASM indices (detailed in Materials and Methods). Because both indices exhibit a high degree of congruence and are statistically positively correlated ($r = 0.55$, $P < 0.05$ for the instrumental period; and $r = 0.68$, $P < 0.05$ for the LM; fig. S10, A and B), we opt to use the precipitation-based SASM index in further analyses (hereafter referred to simply as the SASM index). This index reveals a distinct change in the mean state of the monsoon intensity from the MCA to the LIA. Moreover, the SASM index correlates strongly with the PC of the MVEOF1 mode, as indicated by the significant correlation coefficient of 0.90 ($P < 0.05$; Fig. 2C). Overall, our analysis reveals that the observed centennial-scale shifts seen in $\delta^{18}O$ proxy records from tropical South America, during the transition from the MCA to the LIA, reflect variations in the intensity of the SASM.

Drivers of the SASM

Previous research has identified strong relationships between the variability of the SASM at interannual to multidecadal timescales and the dynamics of regional Walker and Hadley circulations, driven by internally generated coupled ocean-atmosphere variability and associated sea surface temperature anomalies over the tropical Pacific and Atlantic (*26*–*30*). Consequently, to investigate the drivers of centennial-scale fluctuations and trends of the SASM during the transition from the MCA to the LIA, we focus on the relationships between the SASM and both the Pacific Walker circulation (PWC) and the Hadley circulation. To quantitatively assess the intensity of the PWC, we reconstruct the PWC index over the LM, using the sea-level pressure gradient along the equatorial Pacific as a proxy for PWC strength (*31*). In addition, we calculate the mean position of the Atlantic ITCZ based on the latitude of maximum precipitation within the Atlantic tropics (*32*), as detailed in Materials and Methods.

Our analysis demonstrates a significant correlation between the 100-year low-pass–filtered SASM and the PWC index across the LM ($r = 0.76$, $P < 0.05$; Fig. 3A). Both time series exhibit consistent centennial-scale variations, with a minimum during the MCA and a maximum during the LIA, suggesting a strengthening of both the PWC and the SASM during the transition from the MCA to the LIA. Further support for a causal link between these two indices stems from the relationship between the SASM and the vertical velocity averaged across the 5°N to 5°S region. This relationship indicates enhanced upward motion over tropical South America and downward motion over the eastern Pacific (Fig. 3B), which is dynamically consistent with both a stronger PWC and an enhanced SASM. In addition, this finding is corroborated by the composite analysis of atmospheric circulation diagnostics during periods of strong (mostly during the LIA) and weak (mostly during the MCA) SASM events, including the vertical velocity averaged across the 5°N to 5°S region (fig. S9C).

In addition, we find that the centennial-scale variations of the SASM over the LM are significantly correlated with the 100-year low-pass–filtered latitudinal displacement of the Atlantic ITCZ ($r = 0.82$, $P < 0.05$; Fig. 3C). This is consistent with the notable relationship between the 100-year low-pass–filtered SASM index and variations in vertical velocity over the tropical Atlantic (45°W to 10°E) between 10°N and 10°S (Fig. 3D), associated with the Hadley circulation. The observed enhanced upward motion in the 0°S to 10°S range and downward motion in the 0°N to 10°N range suggest a pronounced southward shift of the Atlantic ITCZ concurrent with an intensified SASM. This is further supported by the composite analysis of atmospheric circulation anomalies during strong (mostly during the LIA) and weak (mostly during the MCA) SASM events (fig. S9D).

Our reconstruction uses oxygen isotope records from both the northern and southern hemisphere American Neotropics. It should thus be sensitive to the latitudinal displacements of the Atlantic ITCZ, as suggested by Steinman *et al.* (*33*). Consequently, as expected, our reconstructed Atlantic ITCZ index mirrors the transition from the MCA to the LIA observed in the proxy-based MCEOF1 derived from (*33*) over the LM ($r = 0.72$ at $P < 0.05$; Fig. 4A), although there are methodological, spatial, and data input differences between the two studies. Notably, our results show better consistency with the

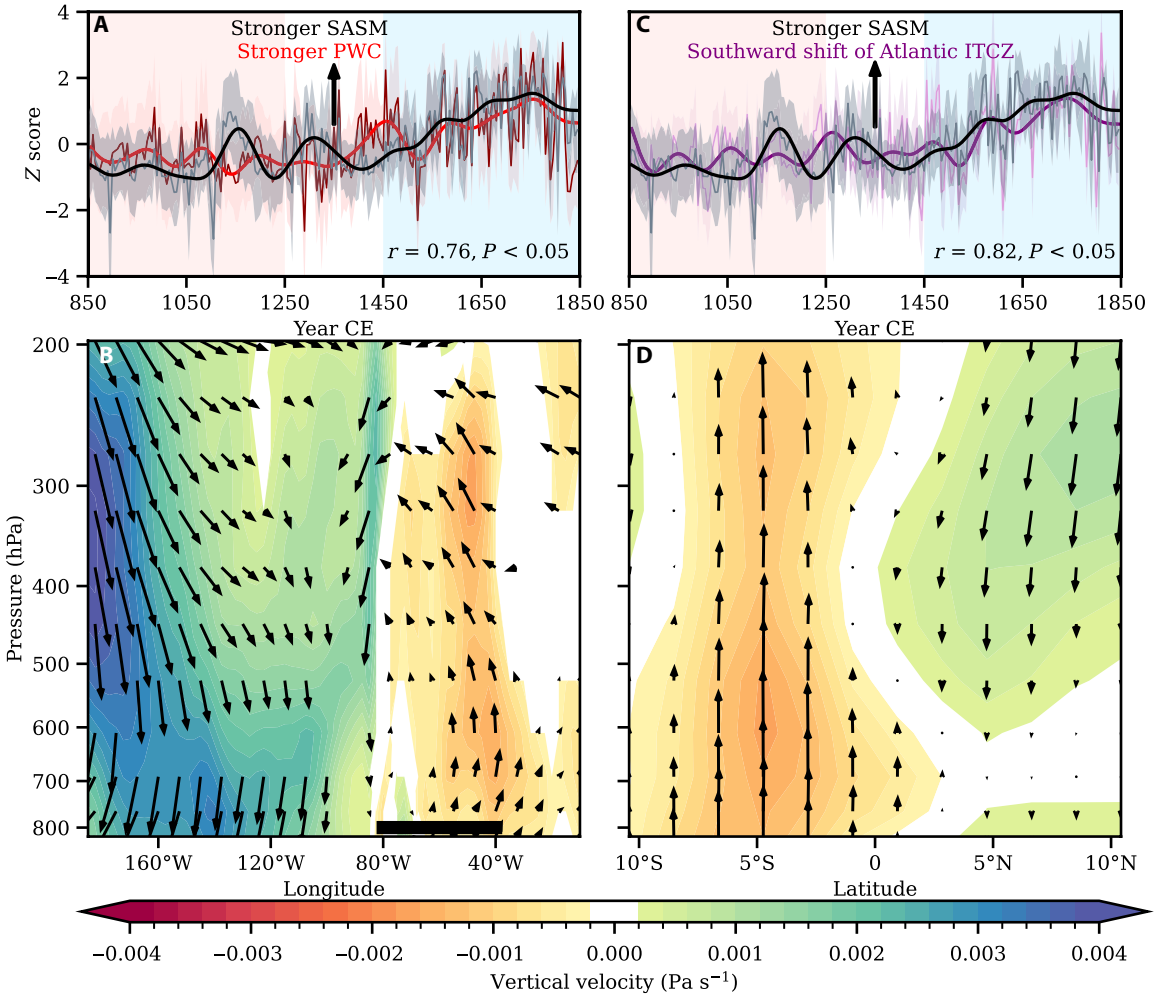

Fig. 3. Relationship between the intensity of the SASM and both the strength of the PWC and the location of the Atlantic ITCZ over the LM. (**A**) DA-reconstructed SASM index and PWC index over the LM. (**B**) Regression of the SASM index against vertical velocity and zonal wind averaged over the latitude band 5°S to 5°N, representative of the PWC. The thick black horizontal bar indicates the location of South America. (**C**) Relationship between the DA- reconstructed Atlantic ITCZ index and the SASM index over the LM. (**D**) Regression of the SASM index against vertical velocity and meridional wind averaged over the tropical Atlantic (45°W to 10°E), representative of the Hadley circulation. Time series in (A) and (C) are depicted with a 5-year average temporal resolution in thinner lines. Shading represents the SD of the ensemble mean from our DA-based reconstruction. Thicker lines represent a 100-year Butterworth low-pass–filtered time series, emphasizing centennial-scale (>100 years) changes. The "*r*" values in (A) and (C) refer to the correlation between the DA-reconstructed 100-year low-pass–filtered SASM index and the PWC index, as well as between the SASM index and the Atlantic ITCZ index. *P* values are estimated using phase-randomization Monte Carlo methods to account for the serial correlation structure of the time series (*81*). Vertical velocity and zonal or meridional wind vectors in (B) and (D) are shown only where the linear regression is significant at the 95% confidence level based on a two-tailed Student's *t* test, with degrees of freedom adjusted for the effective sample size to account for serial correlation in the time series.

titanium (Ti) record from the Cariaco Basin in the southern Caribbean Sea ($r = 0.82$ at $P < 0.05$; Fig. 4B), indicative of Atlantic ITCZ shifts over the LM (*34*) and independent of our DA reconstruction.

The offline DA method used here is able to reconstruct variables not directly assimilated by proxy records through the covariance structures between the reconstructed variables and proxy records as described by the model. Accordingly, the PWC is reconstructed relying on the covariance relationships between the $\delta^{18}O$ records over tropical South America and the PWC, as modeled in the iCESM1, despite the absence of any proxy records from the pan-Pacific domain in our reconstruction. As illustrated in Fig. 4 (C and D), the DA-reconstructed PWC reveals centennial-scale variations that align closely with independent PWC reconstructions over the LM.

Our PWC index exhibits a correlation coefficient of $r = 0.71$ ($P < 0.10$) with the Southern Oscillation Index (SOI) reconstruction by Yan *et al.* (*35*) over the LM (Fig. 4C). Furthermore, there is a strong consistency ($r = 0.87$, $P < 0.05$) between our PWC index and the median of 4800 PWC reconstructions from a global-scale multi-archive compilation of proxy records for the stable isotopic composition of water from 1200 to 1849 CE (Fig. 4D) (*36*). The coefficient of efficiency (*37*) and the correlation coefficient between our reconstruction and the 4800 100-year Butterworth low-pass–filtered PWC reconstructions by Falster *et al.* (*36*) further validate the skill of our reconstruction in capturing centennial variability (fig. S11). Specifically, our reconstruction demonstrates a median of 0.32 for the coefficient of efficiency and a correlation coefficient of 0.64 at

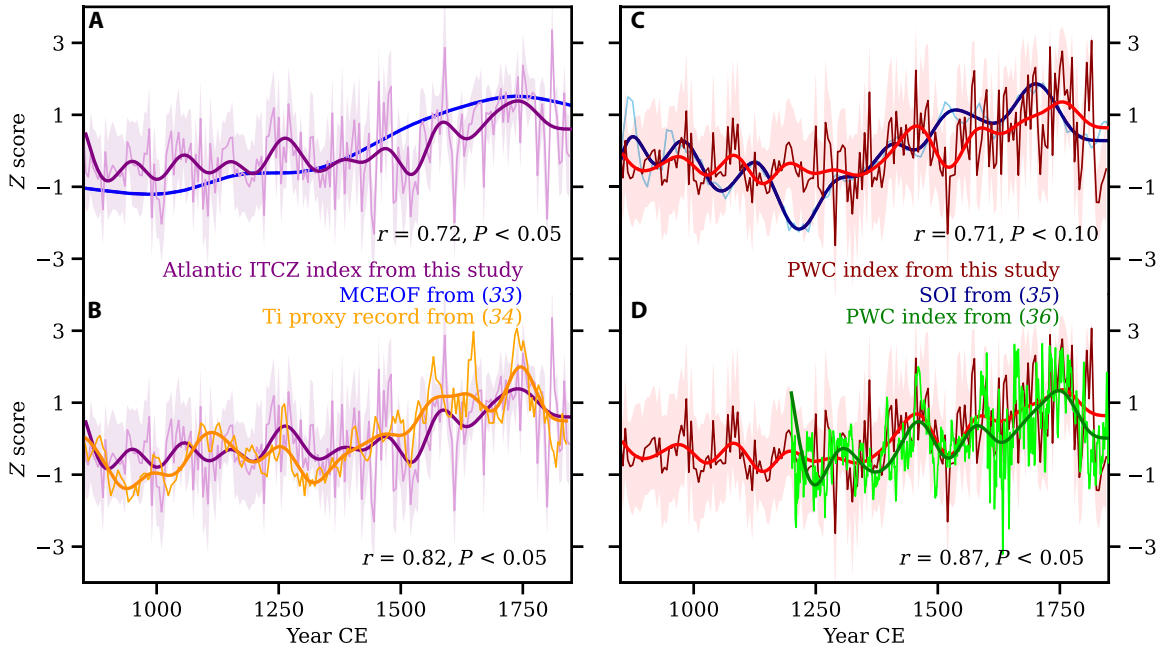

Fig. 4. Validation of the DA reconstruction of the PWC and the Atlantic ITCZ index. (**A** and **B**) Comparison of the DA-reconstructed Atlantic ITCZ index with PC1 of MCEOF1 derived from neotropical hydroclimate records (*33*) and the Cariaco basin titanium (Ti) record derived from (*34*). (**C** and **D**) Comparison of the DA-reconstructed PWC index with the Southern Oscillation index (SOI) reconstruction derived from (*35*) and the PWC index (median) derived from (*36*). In each panel, the thin time series represents the original temporal resolution of the DA reconstruction (i.e., 5-year), as well as the independent Atlantic ITCZ index and the independent PWC (SOI) index. The thicker lines depict the 100-year Butterworth low-pass–filtered results of these datasets. Shading represents the SD of the ensemble mean from our DA-based reconstruction. The *r* values in (A) to (D) refer to the correlation between the respective DA-reconstructed indices and the comparison datasets. *P* values are estimated using phase-randomization Monte Carlo methods to account for the serial correlation structure of the time series (*81*).

$P < 0.05$ among 4800 values, indicating a strong agreement with (*36*). The observed alignment implies a strong covariance between the PWC and $\delta^{18}O$ over tropical South America simulated in iCESM1. This strong covariance, consistent with previous research, demonstrates that iCESM1 accurately captures the diversity of $\delta^{18}O$ anomaly patterns associated with the PWC, as evidenced by the similar $\delta^{18}O$-PWC relationship in both iCESM1 simulations and corresponding observations (*36*, *38*).

While those PWC reconstructions indicate a weakened Walker circulation during the MCA (indicative of an El Niño–like mean state) and a strengthened circulation during the LIA (a La Niña–like mean state), there remains vigorous debate surrounding the mean state of the El Niño–Southern Oscillation over the LM. In particular, hydroclimate records from the western United States (*39*) and sea surface temperature reconstructions from the tropical Pacific (*40*, *41*) suggest a predominance of El Niño–like conditions during the LIA. Nevertheless, there is growing recent evidence for prevalent La Niña–like conditions between the 15th and 17th centuries, such as a multiproxy reconstruction of the NINO3.4 index from the Past Global Changes 2k database (*42*), a PWC reconstruction (*36*), and an Interdecadal Pacific Oscillation index reconstructed from pan-Pacific ice core records (*43*).

DISCUSSION

Our DA approach provides a physically consistent, multivariate, hydroclimatic reconstruction of the SASM through direct assimilation of $\delta^{18}O$ records from the American Neotropics. Compared to previous DA-based reconstructions, such as Paleo Hydrodynamics Data Assimilation (PHYDA) (*44*) and Last Millennium Reanalysis (LMR) (*45*) products, our reconstruction shows more pronounced changes during the transition period from the MCA to the LIA (fig. S12). The PHYDA and LMR do not incorporate most $\delta^{18}O$ records from tropical South America, which contain centennial variability signals related to the SASM. This exclusion explains their damped variability in reconstructing the SASM. Furthermore, the correlation between SASM indices derived from PHYDA and LMR is weak and negative ($r = -0.18$, $P < 0.10$). This indicates that, without the assimilation of $\delta^{18}O$ records from tropical South America, PHYDA and LMR cannot produce robust and consistent SASM reconstructions, despite using the same DA methodology (e.g., ensemble Kalman filter).

Our reconstruction compares well with independent evidence for both $\delta^{18}O$ and precipitation at centennial timescales over the LM. The primary mode of co-variability between $\delta^{18}O$ and precipitation illustrates the joint influence of the amount effect and "upstream" rainout on continental-scale $\delta^{18}O$ over tropical South America. Other more localized synoptic-scale processes, such as air mass mixing, microphysical processes, and local environmental conditions, can substantially alter the $\delta^{18}O$ signal at local scales (*46*–*49*). However, these processes are unlikely to notably alter the first-order, large-scale climate signal at centennial timescales. Because both the prior model (i.e., iCESM1) and the DA-based reconstruction are not able to capture processes that occur at such fine spatial resolution, they are not considered in this study.

Our analysis reveals that the spatially coherent isotopic signal over tropical South America is characterized by increasingly negative

$\delta^{18}O$ values during the transition from the MCA to the LIA. This isotopic signal corresponds with significantly enhanced deep convection over the Amazon region, which can be dynamically interpreted as an intensification of the SASM. This interpretation contrasts with that of Atwood *et al.* (*14*), who suggested that the observed LIA isotopic depletion in the central Andes and southern Amazon reflects upstream rainout in the SASM entrance region rather than a strengthening of the monsoon. Nevertheless, our reconstructed SASM index is significantly correlated with the Atlantic ITCZ index over the LM, indicating that the strengthened SASM and the southward movement of the Atlantic ITCZ likely occurred concurrently during the LIA. Hence, while rainout over both the monsoon entrance region and the core region of convection over the Amazon basin likely contributed to the observed LIA isotopic depletion in the central Andes and southern Amazon, independent non-isotopic proxy records from the western Amazon and the tropical Andes, as well as records related to the movement of the Atlantic ITCZ, indicate wetter conditions and an intensified monsoon, along with a southward shift of the Atlantic ITCZ during the LIA.

The simulations from the Community Earth System Model Last Millennium Ensemble (*50*), despite illustrating a southward shift of the Atlantic ITCZ during the LIA driven by volcanic activity (*33*), fail to adequately replicate the marked hydroclimate transition that occurred in tropical South America from the MCA to the LIA, irrespective of external forcings (fig. S13). This discrepancy may stem from potential model biases, including overlooked feedback mechanisms or uncertainties in convective parameterizations (*15*, *16*). Alternatively, it may suggest that the Atlantic ITCZ shift alone is insufficient to instigate the centennial-scale changes in the SASM that occurred during the transition from the MCA to the LIA. Our study suggests that the dynamic drivers of SASM variability on centennial scales are linked to both the PWC and the Atlantic ITCZ. Notably, our DA-reconstructed PWC, which is strengthened during the LIA (a La Niña–like mean state) compared to the MCA (an El Niño–like mean state), correlates strongly with deep convection over tropical South America. The correlation between the PWC and the SASM observed in this study aligns with the established relationship on interannual timescales, where El Niño events are associated with drier conditions in northeastern Brazil, the central Amazon, and downstream over the tropical Andes (*24*, *51*). However, state-of-the-art climate models display considerable uncertainties in simulating the low-frequency variability of the PWC, attributable to either internal variability or external forcings (*52*–*55*). As a result, attaining reliable PWC projections for the near future constitutes a critical factor for predicting changes in monsoon rainfall over tropical South America.

MATERIALS AND METHODS

Particle filter–based DA

DA is an effective method for integrating observational data with the climate physics represented in climate models. As a methodology of paleoclimate reconstruction, it has several key advantages. First, compared to statistical-based reconstructions, DA reduces the need for an a priori hypothesis regarding the stationarity of the relationship between reconstructed fields and observed variables during a reference period used for calibration, although it still relies on the assumption of stationary covariance structures between climate fields and a consistent signal-to-noise ratio in the observations. Second, it provides a spatially complete estimate for all the variables simulated by the model, allowing for a thorough investigation of the dynamic mechanisms at play (*56*–*59*). In our study, we use an offline approach on the basis of a static ensemble of simulations. This approach uses a particle filter, as outlined by van Leeuwen (*59*) and follows the implementation detailed by Dubinkina *et al.* (*18*), a method having been used in several recent studies (*60*–*62*). The primary motivation for using the particle filter DA approach in our study lies in its ability to handle non-Gaussian statistics and nonlinear dynamics, which are particularly prevalent in the multivariable hydroclimate reconstructions of the SASM through the assimilation of $\delta^{18}O$ proxy records. During the DA process, the likelihood of each ensemble member, or particle, is evaluated by comparing it with the assimilated proxy data. Particles are then assigned weights based on their respective likelihoods, with the weighted average of all particles constituting the DA-based reconstruction. The SD across all particles is used to quantify the uncertainty of the reconstruction at each time step.

The DA framework encompasses three essential elements: (i) prior climate model simulations, (ii) proxy records and their uncertainties, and (iii) proxy system models (PSMs) that establish a connection between climate model output and proxy data. However, we do not incorporate any PSMs in the DA framework for this study. Although some cave drip water $\delta^{18}O$ PSMs, such as Proxy System Modeling tool (PRYSM) (*63*), are accessible, essential parameters like residence time and Peclet number in PRYSM are not yet obtainable from the speleothem sites within our proxy network. Other PSMs to convert $\delta^{18}O_{calcite}$ to $\delta^{18}O_{water}$, such as those recommended by Cauquoin *et al.* (*64*) and Comas-Bru *et al.* (*65*), minimally alter the climatological averages. By comparing the observed $\delta^{18}O_{calcite}$ to $\delta^{18}O_{water}$ where available for the caves over tropical South America, including Huagapo (*66*), Jaragua (*67*), Sao Bernardo-Sao Matheus (*68*), Diva (*69*), and Cuica (*70*), the changes from $\delta^{18}O_{calcite}$ to $\delta^{18}O_{water}$ for the records are as follows: −1.36, 0.71, 1.20, 1.80, and 1.26 per mil (‰), respectively. Because the proxy records that we assimilated are the anomalies respective to a reference period (i.e., the LM) and not the raw data, this small difference in climatology has a minimal impact on our final reconstruction. Nevertheless, we conducted a sensitivity DA experiment using the converted iCESM1-simulated $\delta^{18}O_{calcite}$ as the prior, following the same conversion recommendations of Cauquoin *et al.* (*64*) and Comas-Bru *et al.* (*65*). As expected, the results shown in fig. S14 are virtually identical to our findings.

Prior climate model simulations

The prior model simulations used in DA are derived from three isotope-enabled iCESM1 model simulations (*17*), encompassing the preindustrial era (850 to 1849 CE). These simulations are chosen because they provide a sufficient number of particles to prevent degeneration in the particle filter, as shown in fig. S2. Specifically, they provide at least 600 particles, a particularly vital element when using a 5-year assimilation step (as detailed in the "DA experimental design" section).

Given that oxygen isotope variations are influenced by diverse physical variables, the assessment of the performance of iCESM1 in simulating the near-surface climate over the SASM region is important when using it as the prior in DA. Therefore, we evaluate the iCESM1-simulated 250-hPa geopotential height, precipitation, and precipitation-weighted $\delta^{18}O$ during the austral summer (DJF) by

comparing it to the latest European Centre for Medium-Range Weather Forecasts atmospheric reanalysis v5, ERA5 (*71*), precipitation observations from Global Precipitation Climatology Centre (GPCC) (*72*), and an isotope-enabled reanalysis product from IsoGSM2 (*73*). GPCC is a global rainfall dataset at a resolution of 0.25° longitude × 0.25° latitude with data available from 1891 to the near-present. IsoGSM2 is an isotope-enabled reanalysis product that realistically portrays the $\delta^{18}O$ seasonal cycle and interannual variability in tropical South America with a resolution around 1.6°. These gridded observed datasets have been widely used in climate change studies in South America on timescales ranging from intraseasonal to decadal, e.g., (*3*, *29*).

Averaged over the period 1979 to 2005 CE, the 250-hPa geopotential height simulated in iCESM1 is very close to that in ERA5 over the SASM domain (fig. S3, A and D), exhibiting a bias of less than 40 m compared to that in ERA5, as shown in fig. S3G. This model simulation accurately portrays the Bolivian High, a seasonal upper-level anticyclone forming due to the SASM deep convection over the Amazon basin (*74*). The model also effectively replicates the precipitation-weighted $\delta^{18}O$ continentality gradient from IsoGSM2 during 1980 to 2005 (fig. S3, B and E), displaying the most negative $\delta^{18}O$ values along the Altiplano region and the least negative values along the northeastern South American Atlantic coast. However, the coarse representation of Andean orography in iCESM1 leads to precipitation-weighted $\delta^{18}O$ values that are less negative than in observations, notably over the Altiplano Plateau (with a bias of ~6‰, in fig. S3H). The climatological precipitation patterns simulated by the iCESM1 model are characterized by enhanced precipitation along the eastern slopes of the Andes and in northeastern Brazil (fig. S3F). In contrast, precipitation data observed by GPCC indicate more pronounced maxima within the Amazon Basin (fig. S3C). Notably, the precipitation over the Amazon region as simulated by iCESM1 is ~50 mm/month weaker than the observations reported by GPCC for the period 1979 to 2005. iCESM1 also has some limitations in its ability to capture the location and intensity of the South Atlantic Convergence Zone, a challenge consistent with broader deficiencies observed in global climate models, as noted by Zilli *et al.* (*25*). Nonetheless, given iCESM1's overall skill in simulating the climatology of the SASM, it is well positioned to serve as the prior model for our DA reconstruction.

Proxy records and their uncertainties

In this study, we make use of 18 oxygen isotope records ($\delta^{18}O_{PRECIP}$) derived from three natural archives: ice core (1), lake sediments (1), and speleothems (16). The selected records represent the best available, precisely dated, and high-resolution continental proxies over the American neotropics (details in table S1 and Fig. 1) for reconstructing hydroclimate during the LM (*12*, *30*). Their temporal range covers the LM (850 to 1849 CE), and the time resolution has been interpolated to 1 year, considering the age uncertainty following the methods provided by Tierney *et al.* (*75*) and Orrison *et al.* (*12*).

The uncertainties associated with proxy records are pivotal in DA. Proxy records with low uncertainties carry more weight in DA than those with large uncertainties. This study addresses two types of uncertainties. The first arises from the age uncertainties of each record, which are accounted for using the age model developed by the SISAL project (*76*, *77*). This model uses the Bacon Bayesian method (*78*) to generate an age-depth ensemble comprising 1000 members. Each ensemble member is linearly interpolated between depth-age points and aligned with the depth from each proxy sample to create an ensemble of proxy time series. For samples that do not cover the entire study period, multiple shorter samples are combined to form composite records, following (*12*). The median of the 1000-member ensemble for each proxy record is used in the DA reconstruction. The uncertainty used in DA corresponds to the variance across the 1000 ensemble members at each time step.

The second type of uncertainty relates to unresolved processes at the spatial scale of the proxies due to the model's coarse spatial resolution. This is referred to as a representativeness error. Given the absence of a gridded observational $\delta^{18}O$ dataset with higher spatial resolution than iCESM1, our approach involves using the GPCC dataset to assess representativeness errors. These errors are subsequently converted to $\delta^{18}O$ using the $\delta^{18}O$-precipitation relationship derived from IsoGSM2 via a linear regression conducted over the SASM domain (2.5°S to 18°S and 45°W to 75°W) and the relationship between $\delta^{18}O_{calcite}$ and $\delta^{18}O_{water}$ derived from the PSMs (*64*, *65*). More specifically, we perform spatial smoothing on the original GPCC data, transitioning from its initial resolution of 0.25° × 0.25° to a resolution approximating that of iCESM1 (around 2°) via linear interpolation. Subsequently, we extract the DJF precipitation data within GPCC for the grid cell nearest to each proxy record during the period of 1980 to 2005 CE and, likewise, extract data from the interpolated GPCC at ~2° resolution. We then calculate the variance of the differences within the resulting time series. This value is then multiplied by the $\delta^{18}O$-precipitation relationship derived from IsoGSM2 and the relationship between $\delta^{18}O_{calcite}$ and $\delta^{18}O_{water}$ derived from the PSMs (*64*, *65*) to obtain representativeness errors. Overall, the error applied in the DA is the sum of the first and second errors for each proxy record.

In addition to those records used in the DA, we compile 32 proxy records that are independent of the DA experiment to validate the DA reconstruction. These records are broadly divided into two categories: Proxies recording the stable oxygen isotopic composition of precipitation (referred to as $\delta^{18}O_{PRECIP}$, a to f in Fig. 1A and table S2) and hydroclimatic-sensitive proxy records (referred to as HYDRO records a to z in Fig. 1B and table S3). The $\delta^{18}O_{PRECIP}$ records are used for validation purposes rather than for direct application in the DA reconstruction due to their comparatively lower temporal resolution, approximately on the scale of decades, as opposed to the higher resolution records used in the DA reconstruction. The inclusion criteria for HYDRO records consist of the following:

1) The record is within 0°S to 30°S and 40°W to 80°W.

2) Original studies establish a time frame spanning from 850 to 1849 CE, with a dating error of less than 100 years.

3) Records have at least sub-centennial temporal resolution.

4) Original references clearly indicate that proxy records are associated with changes in precipitation, humidity, or monsoon patterns.

DA experimental design

We assimilate 18 oxygen records derived from speleothems (16), ice core (1), and lake sediments (1), as listed in table S1. The speleothem $\delta^{18}O$ signal is subject to a complex array of factors within the bedrock, such as the mixing of older and younger waters in the epikarst, as well as percolation through distinct flow paths (including fracture flows and matrix flow) (*79*). This complexity means that climatic information is predominantly captured in signals that are temporally

smoothed, typically manifesting on annual to decadal scales. For instance, a residence time of 7 to 9 years was observed in the monitoring program of drip water $\delta^{18}O$ from a cave in the southeastern SASM region (*68*), contrasting with the very short residence time of a few months observed in caves in the western Amazon (*80*). The paucity of such monitoring systems across tropical South America limits our ability to accurately determine the residence time for all speleothem records used in the DA experiment. Consequently, a 5-year average has been used for the oxygen isotope records to reduce the influence of non-climatic signals, such as those stemming from epikarst processes. In addition, we tested a 10-year binning to assess sensitivity to this averaging period. The results, shown in fig. S15, are similar to those with 5-year binning, as presented in Fig. 1.

MVEOF analysis

Empirical orthogonal function (EOF) analysis is a technique that decomposes spatiotemporal input data into temporally varying PCs and spatial patterns by solving an eigenvalue problem. Unlike the conventional EOF method, MVEOF is an advanced extension that constructs a combined matrix for multiple variables (*19*, *20*). MVEOF analysis follows a process by standardizing variables, combining data into a matrix, computing the covariance matrix, performing eigenvalue decomposition, and deriving PC time series. This approach enables the extraction of coupled variability patterns among these variables, offering an advantage in capturing the interactions between different variables. In this study, we use MVEOF analysis to investigate the primary modes of the DA-reconstructed $\delta^{18}O$ and precipitation data. Our focus is on the core monsoon region spanning 2.5°S to 18°S and 45°W to 75°W. The stability of our MVEOF results is confirmed through another sensitivity test, demonstrating that minor adjustments in the analysis region (specifically within 0°S to 25°S and 35°W to 80°W) do not notably affect the outcomes (fig. S16, A and B).

SASM index

To quantitatively evaluate the fluctuations in SASM intensity, we use two distinct methods for calculating the SASM index. The first method involves deriving a vertical wind shear index from the zonal wind at the 850- and 250-hPa levels, averaging over the region 7.5°N to 2.5°S and 45°W to 20°W, as outlined by Vuille and Werner (*24*) and Gan *et al.* (*26*) (referred to here as the wind shear–based SASM index). The second method is based on the total DJF precipitation averaged over the core monsoon region ranging from 2.5°S to 18°S, and 45°W to 75°W) following (*24*) (referred to here as the precipitation-based SASM index). Notably, these two indices demonstrate substantial alignment, as evidenced by significant correlation coefficients of 0.55 ($P < 0.05$) for the instrumental period (fig. S10A) and 0.68 ($P < 0.05$) for the LM from the DA reconstruction (fig. S10B). This consistency across different SASM index definitions underscores the robustness of our findings.

PWC and Atlantic ITCZ index

We calculate the PWC index using the anomalies in the difference between the area-mean sea level pressure over the central eastern Pacific Ocean (160°W to 80°W and 5°S to 5°N) and the western Pacific/eastern Indian Oceans (80°E to 160°E and 5°S to 5°N) following (*31*). The Atlantic ITCZ index is defined as the mean latitude of the Atlantic ITCZ based on the latitude of maximum precipitation within the tropical Atlantic (0°W to 50°W and 10°S to 10°N). Following (*32*), the location of the Atlantic ITCZ is given by expected latitudes, using a weighting function based on the area-weighted precipitation integrated between the latitudes $\emptyset^1$ and $\emptyset^2$

$$\emptyset^{\mathrm{ITCZ}} = \frac{\int_{\emptyset^1}^{\emptyset^2} \phi\left[\cos(\phi)\boldsymbol{P}\right] d\phi}{\int_{\emptyset^1}^{\emptyset^2} \left[\cos(\phi)\boldsymbol{P}\right] d\phi} \quad (1)$$

where $\boldsymbol{P}$ is precipitation, $\emptyset^1 = 10°S$, and $\emptyset^2 = 10°N$. Following (*32*), we interpolate precipitation to a 0.05° resolution to reduce grid dependence. For computational simplicity, all reconstructed indices are directly incorporated into the prior, instead of undergoing post-processing from reconstructed spatial climate fields.

Statistical analysis

To assess linear correlations between variables, the Pearson correlation coefficient was used. However, to accurately determine the reduction in effective degrees of freedom, it is necessary to account for the autocorrelation of the series, particularly in low-pass–filtered time series. To address this, we used phase-randomization Monte Carlo methods as recommended by Ebisuzaki (*81*). This method involves generating 10,000 phase-randomized surrogate time series, calculating Pearson correlation coefficients to form a null distribution, and comparing the observed correlation coefficient to this distribution to estimate the *P* value and determine statistical significance. In addition, for correlations and regression analysis calculated using the 5-year averaged time series (i.e., no low-pass filtering), we applied the two-tailed Student's *t* test, taking into account the effective sample size. Here, the degrees of freedom are chosen on the basis of the effective sample size calculation, which considers the serial correlation in the time series, ensuring the accuracy of the statistical analysis (*82*).

Supplementary Materials

This PDF file includes:

Figs. S1 to S16
Tables S1 to S3
References

REFERENCES AND NOTES

1. C. Vera, W. Higgins, J. Amador, T. Ambrizzi, R. Garreaud, D. Gochis, C. Zhang, Toward a unified view of the American monsoon systems. *J. Clim.* **19**, 4977–5000 (2006).
2. R. D. Garreaud, M. Vuille, R. Compagnucci, J. Marengo, Present-day South American climate. *Palaeogeogr. Palaeoclimatol. Palaeoecol.* **281**, 180–195 (2009).
3. J. A. Marengo, B. Liebmann, A. M. Grimm, V. Misra, P. D. Silva Dias, I. F. A. Cavalcanti, L. M. Alves, Recent developments on the South American monsoon system. *Int. J. Climatol.* **32**, 1–21 (2012).
4. F. Vimeux, R. Gallaire, S. Bony, G. Hoffmann, J. C. Chiang, What are the climate controls on δD in precipitation in the Zongo Valley (Bolivia)? Implications for the Illimani ice core interpretation. *Earth Planet. Sci. Lett.* **240**, 205–220 (2005).
5. M. Vuille, R. S. Bradley, M. Werner, R. Healy, F. Keimig, Modeling $\delta^{18}O$ in precipitation over the tropical Americas: 1. Interannual variability and climatic controls. *J. Geophys. Res.* **108**, 4174 (2003).
6. F. Vimeux, G. Tremoy, C. Risi, R. Gallaire, A strong control of the South American SeeSaw on the intra-seasonal variability of the isotopic composition of precipitation in the Bolivian Andes. *Earth Planet. Sci. Lett.* **307**, 47–58 (2011).
7. L. G. Thompson, E. Mosley-Thompson, M. E. Davis, V. S. Zagorodnov, I. M. Howat, V. N. Mikhalenko, P. N. Lin, Annually resolved ice core records of tropical climate variability over the past 1800 years. *Science* **340**, 945–950 (2013).
8. B. W. Bird, M. B. Abbott, M. Vuille, D. T. Rodbell, N. D. Stansell, M. F. Rosenmeier, A 2300-year-long annually resolved record of the South American summer monsoon from the Peruvian Andes. *Proc. Natl. Acad. Sci. U.S.A.* **108**, 8583–8588 (2011).

9. J. Apaéstegui, F. W. Cruz, A. Sifeddine, M. Vuille, J. C. Espinoza, J. L. Guyot, M. Khodri, N. Strikis, R. V. Santos, H. Cheng, L. Edwards, E. Carvalho, W. Santini, Hydroclimate variability of the northwestern Amazon basin near the Andean foothills of Peru related to the South American Monsoon System during the last 1600 years. *Clim. Past* **10**, 1967–1981 (2014).
10. V. Azevedo, N. M. Strikis, R. A. Santos, J. G. de Souza, A. Ampuero, F. W. Cruz, P. de Oliveira, J. Iriarte, C. F. Stumpf, M. Vuille, V. R. Mendes, H. Cheng, R. L. Edwards, Medieval climate variability in the eastern Amazon-Cerrado regions and its archeological implications. *Sci. Rep.* **9**, 20306 (2019).
11. J. L. P. S. Campos, F. W. Cruz, T. Ambrizzi, M. Deininger, M. Vuille, V. F. Novello, N. M. Stríkis, Coherent South American monsoon variability during the last millennium revealed through high-resolution proxy records. *Geophys. Res. Lett.* **46**, 8261–8270 (2019).
12. R. Orrison, M. Vuille, J. E. Smerdon, J. Apaéstegui, V. Azevedo, J. L. P. Campos, N. M. Stríkis, South American summer monsoon variability over the last millennium in paleoclimate records and isotope-enabled climate models. *Clim. Past* **18**, 2045–2062 (2022).
13. M. Vuille, S. J. Burns, B. L. Taylor, F. W. Cruz, B. W. Bird, M. B. Abbott, V. F. Novello, A review of the South American monsoon history as recorded in stable isotopic proxies over the past two millennia. *Clim. Past* **8**, 1309–1321 (2012).
14. A. R. Atwood, D. S. Battisti, E. Wu, D. M. W. Frierson, J. P. Sachs, Data-model comparisons of tropical hydroclimate changes over the common era. *Paleoceanogr. Paleoclimatol.* **36**, e2020PA003934 (2021).
15. J. C. Bühler, J. Axelsson, F. A. Lechleitner, J. Fohlmeister, A. N. LeGrande, M. Midhun, K. Rehfeld, Investigating stable oxygen and carbon isotopic variability in speleothem records over the last millennium using multiple isotope-enabled climate models. *Clim. Past* **18**, 1625–1654 (2022).
16. M. Rojas, P. A. Arias, V. Flores-Aqueveque, A. Seth, M. Vuille, The South American monsoon variability over the last millennium in climate models. *Clim. Past* **12**, 1681–1691 (2016).
17. E. Brady, S. Stevenson, D. Bailey, Z. Liu, D. Noone, J. Nusbaumer, J. Zhu, The connected isotopic water cycle in the Community Earth System Model version 1. *J. Adv. Model. Earth Syst.* **11**, 2547–2566 (2019).
18. S. Dubinkina, H. Goosse, Y. Sallaz-Damaz, E. Crespin, M. Crucifix, Testing a particle filter to reconstruct climate changes over the past centuries. *Int. J. Bifurcation Chaos* **21**, 3611–3616 (2011).
19. B. Wang, The vertical structure and development of the ENSO anomaly mode during 1979-1989. *J. Atmos. Sci.* **49**, 698–712 (1992).
20. J. E. Kutzbach, Empirical eigenvectors of sea-level pressure, surface temperature and precipitation complexes over North America. *J. Appl. Meteorol. Climatol.* **6**, 791–802 (1967).
21. W. Dansgaard, Stable isotopes in precipitation. *Tellus* **16**, 436–468 (1964).
22. G. Hoffmann, E. Ramirez, J. D. Taupin, B. Francou, P. Ribstein, R. Delmas, M. Werner, Coherent isotope history of Andean ice cores over the last century. *Geophys. Res. Lett.* **30**, 1179 (2003).
23. J. C. A. Baker, M. Gloor, D. V. Spracklen, S. R. Arnold, J. C. Tindall, S. J. Clerici, R. J. W. Brienen, What drives interannual variation in tree ring oxygen isotopes in the Amazon? *Geophys. Res. Lett.* **43**, 11831–11840 (2016).
24. M. Vuille, M. Werner, Stable isotopes in precipitation recording South American summer monsoon and ENSO variability: Observations and model results. *Climate Dynam.* **25**, 401–413 (2005).
25. M. T. Zilli, L. M. Carvalho, B. R. Lintner, The poleward shift of South Atlantic convergence zone in recent decades. *Climate Dynam.* **52**, 2545–2563 (2019).
26. M. A. Gan, V. E. Kousky, C. F. Ropelewski, The South America monsoon circulation and its relationship to rainfall over west-central Brazil. *J. Clim.* **17**, 47–66 (2004).
27. L. M. Carvalho, C. Jones, A. N. Posadas, R. Quiroz, B. Bookhagen, B. Liebmann, Precipitation characteristics of the South American monsoon system derived from multiple datasets. *J. Clim.* **25**, 4600–4620 (2012).
28. J. Barichivich, E. Gloor, P. Peylin, R. J. Schöngart, J. C. Espinoza, K. C. Pattnayak, Recent intensification of Amazon flooding extremes driven by strengthened Walker circulation. *Sci. Adv.* **4**, eaat8785 (2018).
29. Z. He, A. Dai, M. Vuille, The joint impacts of Atlantic and Pacific multidecadal variability on South American precipitation and temperature. *J. Clim.* **34**, 7959–7981 (2021).
30. J. Sulca, M. Vuille, B. Dong, Interdecadal variability of the austral summer precipitation over the Central Andes. *Front. Earth Sci.* **10**, 954954 (2022).
31. G. A. Vecchi, B. J. Soden, Global warming and the weakening of the tropical circulation. *J. Clim.* **20**, 4316–4340 (2007).
32. O. Adam, T. Bischoff, T. Schneider, Seasonal and interannual variations of the energy flux equator and ITCZ. Part I: Zonally averaged ITCZ position. *J. Clim.* **29**, 3219–3230 (2016).
33. B. A. Steinman, N. D. Stansell, M. E. Mann, C. A. Cooke, M. B. Abbott, M. Vuille, A. Fernandez, Interhemispheric antiphasing of neotropical precipitation during the past millennium. *Proc. Natl. Acad. Sci. U.S.A.* **119**, e2120015119 (2022).
34. G. H. Haug, K. A. Hughen, D. M. Sigman, L. C. Peterson, U. Rohl, Southward migration of the intertropical convergence zone through the Holocene. *Science* **293**, 1304–1308 (2001).
35. H. Yan, L. Sun, Y. Wang, W. Huang, S. Qiu, C. Yang, A record of the Southern Oscillation Index for the past 2000 years from precipitation proxies. *Nat. Geosci.* **4**, 611–614 (2011).
36. G. Falster, B. Konecky, S. Coats, S. Stevenson, Forced changes in the Pacific Walker circulation over the past millennium. *Nature* **622**, 93–100 (2023).
37. J. E. Nash, J. V. Sutcliffe, River flow forecasting through conceptual models part I—A discussion of principles. *J. Hydrol.* **10**, 282–290 (1970).
38. G. Falster, B. Konecky, M. Madhavan, S. Stevenson, S. Coats, Imprint of the Pacific Walker circulation in global precipitation $\delta^{18}O$. *J. Clim.* **34**, 8579–8597 (2021).
39. E. R. Cook, C. A. Woodhouse, C. M. Eakin, D. M. Meko, D. W. Stahle, Long-term aridity changes in the western United States. *Science* **306**, 1015–1018 (2004).
40. K. M. Cobb, C. D. Charles, H. Cheng, R. L. Edwards, El Niño/Southern Oscillation and tropical Pacific climate during the last millennium. *Nature* **424**, 271–276 (2003).
41. G. T. Rustic, A. Koutavas, T. M. Marchitto, B. K. Linsley, Dynamical excitation of the tropical Pacific Ocean and ENSO variability by Little Ice Age cooling. *Science* **350**, 1537–1541 (2015).
42. T. Delcroix, S. L. L. Michel, D. Swingedouw, B. Malaizé, A. L. Daniau, R. Abarca-del-Rio, A. M. Sémah, Clarifying the role of ENSO on Easter Island precipitation changes: Potential environmental implications for the last millennium. *Paleoceanogr. Paleoclimatol.* **37**, e2022PA004514 (2022).
43. S. E. Porter, E. Mosley-Thompson, L. G. Thompson, A. B. Wilson, Reconstructing an interdecadal Pacific oscillation index from a Pacific basin-wide collection of ice core records. *J. Clim.* **34**, 3839–3385 (2021).
44. N. J. Steiger, J. E. Smerdon, R. Seager, A. P. Williams, A. M. Varuolo-Clarke, ENSO-driven coupled megadroughts in North and South America over the last millennium. *Nat. Geosci.* **14**, 739–744 (2021).
45. R. Tardif, G. J. Hakim, W. A. Perkins, K. A. Horlick, M. P. Erb, J. Emile-Geay, D. M. Anderson, E. J. Steig, D. Noone, Last Millennium Reanalysis with an expanded proxy database and seasonal proxy modeling. *Clim. Past* **15**, 1251–1273 (2019).
46. C. Risi, S. Bony, F. Vimeux, Influence of convective processes on the isotopic composition ($\delta^{18}O$ and δD) of precipitation and water vapor in the tropics: 2. Physical interpretation of the amount effect. *J. Geophys. Res. Atmos.* **113**, D19306 (2008).
47. B. L. Konecky, D. C. Noone, K. M. Cobb, The influence of competing hydroclimate processes on stable isotope ratios in tropical rainfall. *Geophys. Res. Lett.* **46**, 1622–1633 (2019).
48. A. Ampuero, N. M. Stríkis, J. Apaéstegui, M. Vuille, V. F. Novello, J. C. Espinoza, F. W. Cruz, H. Vonhof, V. C. Mayta, V. T. S. Martins, R. C. Corderio, V. Azevedo, A. Sifeddine, The forest effects on the isotopic composition of rainfall in the northwestern Amazon Basin. *J. Geophys. Res. Atmos.* **125**, e2019JD031445 (2020).
49. J. Hu, J. Emile-Geay, C. Tabor, J. Nusbaumer, J. Partin, Deciphering oxygen isotope records from Chinese speleothems with an isotope-enabled climate model. *Paleoceanogr. Paleoclimatol.* **34**, 2098–2112 (2019).
50. B. L. Otto-Bliesner, E. C. Brady, J. Fasullo, A. Jahn, L. Landrum, S. Stevenson, N. Rosenbloom, A. Mai, G. Strand, Climate variability and change since 850 CE: An ensemble approach with the Community Earth System Model. *Bull. Am. Meteorol. Soc.* **97**, 735–754 (2016).
51. W. Cai, M. McPhaden, A. Grimm, R. Rodrigues, A. Taschetto, R. Garreaud, B. Dewitte, G. Poveda, Y.-G. Ham, A. Santoso, B. Ng, W. Anderson, G. Wang, T. Geng, H.-S. Jo, J. Marengo, L. Alves, M. Osman, S. Li, C. Vera, Climate impacts of the El Niño-Southern Oscillation on South America. *Nat. Rev. Earth Environ.* **1**, 215–231 (2020).
52. R. C. Wills, Y. Dong, C. Proistosecu, K. C. Armour, D. S. Battisti, Systematic climate model biases in the large-scale patterns of recent sea-surface temperature and sea-level pressure change. *Geophys. Res. Lett.* **49**, e2022GL100011 (2022).
53. A. T. Wittenberg, Are historical records sufficient to constrain ENSO simulations? *Geophys. Res. Lett.* **36**, L12702 (2009).
54. M. Collins, S. I. An, W. Cai, A. Ganachaud, E. Guilyardi, F. F. Jin, M. Jochum, M. Lengaigne, S. Power, A. Timmermann, G. Vecchi, The impact of global warming on the tropical Pacific Ocean and El Niño. *Nat. Geosci.* **3**, 391–397 (2010).
55. G. A. Vecchi, B. J. Soden, A. T. Wittenberg, I. M. Held, A. Leetmaa, M. J. Harrison, Weakening of tropical Pacific atmospheric circulation due to anthropogenic forcing. *Nature* **441**, 73–76 (2006).
56. H. Goosse, E. Crespin, A. de Montety, M. E. Mann, H. Renssen, A. Timmermann, Reconstructing surface temperature changes over the past 600 years using climate model simulations with data assimilation. *J. Geophys. Res. Atmos.* **115**, D09108 (2010).
57. M. Widmann, H. Goosse, G. van der Schrier, R. Schnur, J. Barkmeijer, Using data assimilation to study extratropical Northern Hemisphere climate over the last millennium. *Clim. Past* **6**, 627–644 (2010).
58. G. J. Hakim, J. Emile-Geay, E. J. Steig, D. Noone, D. M. Anderson, R. Tardif, W. A. Perkins, The last millennium climate reanalysis project: Framework and first results. *J. Geophys. Res. Atmos.* **121**, 6745–6764 (2016).

59. P. J. Van Leeuwen, Particle filtering in geophysical systems. *Mon. Wea. Rev.* **137**, 4089–4114 (2009).
60. Z. Lyu, H. Goosse, Q. Dalaiden, F. Klein, F. Shi, S. Wagner, P. Braconnot, Spatial patterns of multi-centennial surface air temperature trends in Antarctica over 1-1000 CE: Insights from ice core records and modeling. *Quat. Sci. Rev.* **271**, 107205 (2021).
61. Q. Dalaiden, J. Rezsöhazy, H. Goosse, E. R. Thomas, D. O. Vladimirova, D. Tetzner, An unprecedented sea ice retreat in the Weddell Sea driving an overall decrease of the Antarctic Sea-ice extent over the 20th century. *Geophys. Res. Lett.* **50**, e2023GL104666 (2023).
62. Q. Dalaiden, H. Goosse, J. Rezsöhazy, E. R. Thomas, Reconstructing atmospheric circulation and sea-ice extent in the West Antarctic over the past 200 years using data assimilation. *Climate Dynam.* **57**, 3479–3503 (2021).
63. S. Dee, J. Emile-Geay, M. N. Evans, A. Allam, E. J. Steig, D. M. Thompson, PRYSM: An open-source framework for PRoxy System Modeling, with applications to oxygen-isotope systems. *J. Adv. Model. Earth Syst.* **7**, 1220–1247 (2015).
64. A. Cauquoin, M. Werner, G. Lohmann, Water isotopes-climate relationships for the mid-Holocene and preindustrial period simulated with an isotope-enabled version of MPI-ESM. *Clim. Past* **15**, 1913–1937 (2019).
65. L. Comas-Bru, S. P. Harrison, M. Werner, K. Rehfeld, N. Scroxton, C. Veiga-Pires, SISAL working group members: Evaluating model outputs using integrated global speleothem records of climate change since the last glacial. *Clim. Past* **15**, 1557–1579 (2019).
66. L. C. Kanner, S. J. Burns, H. Cheng, R. L. Edwards, M. Vuille, High-resolution variability of the South American summer monsoon over the last seven millennia: Insights from a speleothem record from the central Peruvian Andes. *Quat. Sci. Rev.* **75**, 1–10 (2013).
67. V. F. Novello, F. W. Cruz, J. S. Moquet, M. Vuille, M. S. De Paula, D. Nunes, R. L. Edwards, H. Cheng, I. Karmann, G. Utida, N. M. Stríkis, Two millennia of South Atlantic convergence zone variability reconstructed from isotopic proxies. *Geophys. Res. Lett.* **45**, 5045–5051 (2018).
68. J. S. Moquet, F. W. Cruz, V. F. Novello, N. M. Strikis, M. Deininger, I. Karmann, R. V. Santos, C. Millo, J. Apaéstegui, J. L. Guyot, A. Siffedine, M. Vuille, H. Cheng, R. L. Edwards, W. Santini, Calibration of speleothem $\delta^{18}O$ records against hydroclimate instrumental records in Central Brazil. *Glob. Planet. Change* **139**, 151–164 (2016).
69. V. F. Novello, F. W. Cruz, I. Karmann, S. J. Burns, N. M. Strikis, M. Vuille, H. Cheng, R. Lawrence-Edwards, R. V. Santos, E. Frigo, E. A. S. Barreto, Multidecadal climate variability in Brazil's Nordeste during the last 3000 years based on speleothem isotope records. *Geophys. Res. Lett.* **39**, L23706 (2012).
70. M. E. Della Libera, V. F. Novello, F. W. Cruz, R. Orrison, M. Vuille, S. Y. Maezumi, J. de Souza, J. Cauhy, J. L. P. S. Campos, A. Ampuero, G. Utida, N. M. Strikis, C. F. Stumpf, V. Azevedo, H. Zhang, R. L. Edwards, H. Cheng, Paleoclimatic and paleoenvironmental changes in Amazonian lowlands over the last three millennia. *Quat. Sci. Rev.* **279**, 107383 (2022).
71. H. Hersbach, B. Bell, P. Berrisford, S. Hirahara, A. Horányi, J. Muñoz-Sabater, J. Nicolas, C. Peubey, R. Radu, D. Schepers, A. Simmons, The ERA5 global reanalysis. *Q. J. Roy. Meteorol. Soc.* **146**, 1999–2049 (2020).
72. U. Schneider, A. Becker, P. Finger, A. Meyer-Christoffer, B. Rudolf, M. Ziese, "GPCC full data reanalysis version 6.0 at 0.5°: Monthly land-surface precipitation from rain-gauges built on GTS-based and historic data" (GPCC Data Report, 2011).
73. K. Yoshimura, M. Kanamitsu, D. Noone, T. Oki, Historical isotope simulation using Reanalysis atmospheric data. *J. Geophys. Res.* **113**, 1–15 (2008).
74. J. D. Lenters, K. H. Cook, On the origin of the Bolivian high and related circulation features of the South American climate. *J. Atmos. Sci.* **54**, 656–677 (1997).
75. J. E. Tierney, J. Zhu, J. King, S. B. Malevich, G. J. Hakim, C. J. Poulsen, Glacial cooling and climate sensitivity revisited. *Nature* **584**, 569–573 (2020).
76. N. Kaushal, F. A. Lechleitner, M. Wilhelm, K. Azennoud, J. C. Bühler, K. Braun, Y. A. Brahim, S. M. Ahmad, A. Baker, M. Bosomworth, S. F. M. Breitenbach, Y. Burstyn, A. Columbu, M. Deininger, A. Demény, B. Dixon, J. Fohlmeister, I. G. Hatvani, J. Hu, Z. Kern, I. Labuhn, A. Lorrey, B. Martrat, V. F. Novello, J. Oster, C. Pérez-Mejías, D. Scholz, N. Scroxton, B. M. Ward, S. Warken, H. Zhang, SISALv3: A global speleothem stable isotope and trace element database. *Earth Syst. Sci. Data* **16**, 1933–1963 (2024).
77. L. Comas-Bru, K. Rehfeld, C. Roesch, S. Amirnezhad-Mozhdehi, S. P. Harrison, K. Atsawawaranunt, S. M. Ahmad, Y. A. Brahim, A. Baker, M. Bosomworth, S. F. M. Breitenbach, Y. Burstyn, A. Columbu, M. Deininger, A. Demény, B. Dixon, J. Fohlmeister, I. G. Hatvani, J. Hu, N. Kaushal, Z. Kern, I. Labuhn, F. A. Lechleitner, A. Lorrey, B. Martrat, V. F. Novello, J. Oster, C. Pérez-Mejías, D. Scholz, N. Scroxton, N. Sinha, B. M. Ward, S. Warken, H. Zhang, SISALv2: A comprehensive speleothem isotope database with multiple age-depth models. *Earth Syst. Sci. Data* **12**, 2579–2606 (2020).
78. M. Blaauw, J. A. Christen, Flexible paleoclimate age-depth models using an autoregressive gamma process. *Bayesian Anal.* **6**, 457–474 (2011).
79. J. Hu, S. G. Dee, C. I. Wong, C. J. Harman, J. L. Banner, K. E. Bunnell, Assessing proxy system models of cave dripwater $\delta^{18}O$ variability. *Quat. Sci. Rev.* **254**, 106799 (2021).
80. A. Jiménez-Iñiguez, A. Ampuero, B. G. Valencia, V. C. Mayta, F. W. Cruz, M. Vuille, V. F. Novello, N. M. Stríkis, N. Aranda, B. Conicelli, Stable isotope variability of precipitation and cave drip-water at Jumandy cave, western Amazon River basin (Ecuador). *J. Hydrol.* **610**, 127848 (2022).
81. W. Ebisuzaki, A method to estimate the statistical significance of a correlation when the data are serially correlated. *J. Clim.* **10**, 2147–2153 (1997).
82. S. Bretherton, M. Widmann, V. P. Dymnikov, J. M. Wallace, I. Bladé, The effective number of spatial degrees of freedom of a time-varying field. *J. Clim.* **12**, 1990–2009 (1999).
83. C. Funk, P. Peterson, M. Landsfeld, D. Pedreros, J. Verdin, S. Shukla, The climate hazards infrared precipitation with stations—A new environmental record for monitoring extremes. *Sci. Data* **2**, 150066 (2015).
84. B. E. Wortham, C. I. Wong, L. C. Silva, D. McGee, I. P. Montañez, E. T. Rasbury, K. M. Cooper, W. D. Sharp, J. J. Glessner, R. V. Santos, Assessing response of local moisture conditions in central Brazil to variability in regional monsoon intensity using speleothem $^{87}Sr/^{86}Sr$ values. *Earth Planet. Sci. Lett.* **463**, 310–322 (2017).
85. V. F. Novello, M. Vuille, F. W. Cruz, N. M. Strikis, M. S. De Paula, R. L. Edwards, H. Cheng, I. Karmann, P. F. Jaqueto, R. I. F. Trindade, G. A. Hartmann, J. S. Moquet, Centennial-scale solar forcing of the South American Monsoon System recorded in stalagmites. *Sci. Rep.* **6**, 24762 (2016).
86. J. Fohlmeister, N. R. G. Voarintsoa, F. A. Lechleitner, M. Boyd, S. Brandtstätter, M. J. Jacobson, J. Oster, Main controls on the stable carbon isotope composition of speleothems. *Geochim. Cosmochim. Acta.* **279**, 67–87 (2020).
87. X. Wang, R. L. Edwards, A. S. Auler, H. Cheng, X. Kong, Y. Wang, F. W. Cruz, J. A. Dorale, H. W. Chiang, Hydroclimate changes across the Amazon lowlands over the past 45000 years. *Nature* **541**, 204–207 (2017).
88. C. Fensterer, D. Scholz, D. L. Hoffmann, C. Spötl, A. Schröder-Ritzrau, C. Horn, J. M. Pajon, A. Mangini, Millennial-scale climate variability during the last 12.5 ka recorded in a Caribbean speleothem. *Earth Planet. Sci. Lett.* **361**, 143–151 (2013).
89. M. S. Lachniet, J. P. Bernal, Y. Asmerom, V. Polyak, D. Piperno, A 2400 yr Mesoamerican rainfall reconstruction links climate and cultural change. *Geology* **40**, 259–262 (2012).
90. P. D. Akers, G. A. Brook, L. B. Railsback, F. Liang, G. Iannone, J. W. Webster, P. P. Reeder, H. Cheng, R. L. Edwards, An extended and higher-resolution record of climate and land use from stalagmite MC01 from Macal Chasm, Belize, revealing connections between major dry events, overall climate variability, and Maya sociopolitical changes. *Palaeogeogr. Palaeoclimatol. Palaeoecol.* **459**, 268–288 (2016).
91. A. Winter, T. Miller, Y. Kushnir, A. Sinha, A. Timmermann, M. R. Jury, C. Gallup, H. Cheng, R. L. Edwards, Evidence for 800 years of North Atlantic multi-decadal variability from a Puerto Rican speleothem. *Earth Planet. Sci. Lett.* **308**, 23–28 (2011).
92. M. Medina-Elizalde, S. J. Burns, D. W. Lea, Y. Asmerom, L. von Gunten, V. Polyak, M. Vuille, A. Karmalkar, High resolution stalagmite climate record from the Yucatán Peninsula spanning the Maya terminal classic period. *Earth Planet. Sci. Lett.* **298**, 255–262 (2010).
93. J. C. Rodrigues, "Paleoclimate reconstruction based on high-resolution multiproxy geochemistry of speleothems from Paraná and São Paulo states, Brazil," thesis, Universidade de São Paulo, 2020.
94. L. G. Thompson, E. Mosley-Thompson, M. E. Davis, P.-N. Lin, K. A. Henderson, J. Cole-Dai, J. F. Bolzan, K.-B. Liu, Late Glacial Stage and Holocene tropical ice core records from Huascarán, Peru. *Science* **269**, 46–50 (1995).
95. M. L. Wong, X. Wang, E. M. Latrubesse, S. He, M. Bayer, Variations in the South Atlantic Convergence Zone over the mid-to-late Holocene inferred from speleothem $\delta^{18}O$ in central Brazil. *Quat. Sci. Rev.* **270**, 107178 (2021).
96. L. G. Thompson, M. E. Davis, E. Mosley-Thompson, T. A. Sowers, K. A. Henderson, V. S. Zagorodnov, P. N. Lin, V. N. Mikhalenko, R. K. Campen, J. F. Bolzan, J. Cole-Dai, A 25000-year tropical climate history from Bolivian ice cores. *Science* **282**, 1858–1864 (1998).
97. G. Utida, F. W. Cruz, J. Etourneau, I. Bouloubassi, E. Schefuß, M. Vuille, V. F. Novello, L. F. Prado, A. Sifeddine, V. Klein, A. Zular, Tropical South Atlantic influence on Northeastern Brazil precipitation and ITCZ displacement during the past 2300 years. *Sci. Rep.* **9**, 1698 (2019).
98. I. A. Jara, A. Maldonado, M. E. de Porras, Late Holocene dynamics of the South American summer monsoon: New insights from the Andes of northern Chile (21°S). *Quat. Sci. Rev.* **246**, 106533 (2020).
99. G. Utida, F. W. Cruz, M. Vuille, A. Ampuero, V. F. Novello, J. Maksic, G. Sampaio, H. Cheng, H. Zhang, F. R. Dias de Andrade, R. L. Edwards, Spatiotemporal Intertropical Convergence Zone dynamics during the last 3 millennia in northeastern Brazil and related impacts in modern human history. *Clim. Past* **19**, 1975–1992 (2023).
100. N. Michelutti, P. M. Tapia, C. Grooms, A. L. Labaj, J. P. Smol, Differing limnological responses to late Holocene climate variability in the Cordillera Vilcanota, Peruvian Andes. *J. Paleolimnol.* **64**, 121–135 (2020).
101. B. Zolitschka, A. S. Lee, D. P. Bermúdez, T. Giesecke, Environmental variability at the margin of the South American monsoon system recorded by a high-resolution sediment record from Lagoa Dourada (South Brazil). *Quat. Sci. Rev.* **272**, 107204 (2021).
102. S. Guédron, C. Delaere, S. C. Fritz, J. Tolu, P. Sabatier, A. L. Devel, C. Heredia, C. Vérin, E. Q. Alves, P. A. Baker, Holocene variations in Lake Titicaca water level and their implications for sociopolitical developments in the central Andes. *Proc. Natl. Acad. Sci. U.S.A.* **120**, e2215882120 (2023).

103. C. M. Åkesson, C. N. McMichael, S. León-Yánez, M. B. Bush, Late-Holocene maize cultivation, fire, and forest change at Lake Ayauchi, Amazonian Ecuador. *Holocene* **33**, 550–561 (2023).
104. C. Åkesson, C. N. H. McMichael, M. F. Raczka, S. N. Huisman, M. Palmeira, J. Vogel, D. Neill, J. Veizaj, M. B. Bush, Long-term ecological legacies in western Amazonia. *J. Ecol.* **109**, 432–446 (2021).
105. F. Matthews-Bird, B. G. Valencia, W. Church, L. C. Peterson, M. Bush, A 2000-year history of disturbance and recovery at a sacred site in Peru's northeastern cloud forest. *Holocene* **27**, 1707–1719 (2017).
106. M. B. Bush, A. Correa-Metrio, C. H. McMichael, S. Sully, C. R. Shadik, B. G. Valencia, T. Guilderson, M. Steinitz-Kannan, J. T. Overpeck, A 6900-year history of landscape modification by humans in lowland Amazonia. *Quat. Sci. Rev.* **141**, 52–64 (2016).
107. Z. Engel, G. Skrzypek, T. Chuman, L. Šefrna, M. Mihaljevič, Climate in the Western Cordillera of the Central Andes over the last 4300 years. *Quat. Sci. Rev.* **99**, 60–77 (2014).
108. S. Y. Maezumi, D. Alves, M. Robinson, J. G. de Souza, C. Levis, R. L. Barnett, E. Almeida de Oliveira, D. Urrego, D. Schaan, J. Iriarte, The legacy of 4,500 years of polyculture agroforestry in the eastern Amazon. *Nat. Plants* **4**, 540–547 (2018).
109. J. F. Carson, B. S. Whitney, F. E. Mayle, J. Iriarte, H. Prümers, J. D. Soto, J. Watling, Environmental impact of geometric earthwork construction in pre-Columbian Amazonia. *Proc. Natl. Acad. Sci. U.S.A.* **111**, 10497–10502 (2014).
110. K. Schittek, M. Forbriger, D. Berg, J. Hense, F. Schäbitz, B. Eitel, Last millennial environmental dynamics in the western Peruvian Andes inferred from the development of a cushion-plant peat hillock. *Perspect. Plant Ecol. Evol. Syst.* **30**, 115–124 (2018).
111. S. O. Brugger, E. Gobet, J. F. N. van Leeuwen, M.-P. Ledru, D. Colombaroli, W. O. van der Knaap, U. Lombardo, K. Escobar-Torrez, W. Finsinger, L. Rodrigues, A. Giesche, M. Zarate, H. Veit, W. Tinner, Long-term man-environment interactions in the Bolivian Amazon: 8000 years of vegetation dynamics. *Quat. Sci. Rev.* **132**, 114–128 (2016).
112. G. M. Cárdenes-Sandí, "Reconstrucción del escenario ambiental durante los últimos la cuenca del Lago Limón, 2200 años de la zona de Amazonía Peruana," thesis, Universidad de Costa Rica, 2011.
113. T. J. Kelly, I. T. Lawson, K. H. Roucoux, T. R. Baker, E. N. Honorio-Coronado, T. D. Jones, S. Rivas Panduro, Continuous human presence without extensive reductions in forest cover over the past 2500 years in an aseasonal Amazonian rainforest. *J. Quat. Sci.* **33**, 369–379 (2018).
114. M. N. Nascimento, G. S. Martins, R. C. Cordeiro, B. Turcq, L. S. Moreira, M. B. Bush, Vegetation response to climatic changes in western Amazonia over the last 7,600 years. *J. Biogeogr.* **46**, 2389–2406 (2019).
115. C. M. Moy, G. O. Seltzer, D. T. Rodbell, D. M. Anderson, Variability of El Niño/Southern Oscillation activity at millennial timescales during the Holocene epoch. *Nature* **420**, 162–165 (2002).
116. L. G. Thompson, E. Mosley-Thompson, J. F. Bolzan, B. R. Koci, A 1500-year record of tropical precipitation in ice cores from the Quelccaya Ice Cap, Peru. *Science* **229**, 971–973 (1985).
117. M. W. Binford, A. L. Kolata, M. Brenner, J. W. Janusek, M. T. Seddon, M. Abbott, J. H. Curtis, Climate variation and the rise and fall of an Andean civilization. *Quat. Res.* **47**, 235–248 (1997).
118. J. Schellekens, I. Horak-Terra, P. Buurman, A. C. Silva, P. Vidal-Torrado, Holocene vegetation and fire dynamics in central-eastern Brazil: Molecular records from the Pau de Fruta peatland. *Org. Geochem.* **77**, 32–42 (2014).
119. I. Horák-Terra, A. Martínez Cortizas, C. F. P. da Luz, P. Rivas López, A. C. Silva, P. Vidal-Torrado, Holocene climate change in central-eastern Brazil reconstructed using pollen and geochemical records of Pau de Fruta mire (Serra do Espinhaço Meridional, Minas Gerais). *Palaeogeogr. Palaeoclimatol. Palaeoecol.* **437**, 117–131 (2015).
120. A. Bahr, S. Kaboth-Bahr, A. Jaeschke, C. Chiessi, F. Cruz, L. Carvalho, O. Friedrich, Late Holocene precipitation fluctuations in South America triggered by variability of the North Atlantic overturning circulation. *Paleoceanogr. Paleoclimatol.* **36**, e2021PA004223 (2021).

Acknowledgments: We thank the reviewers for insightful comments, which have significantly improved the paper. Z.L. acknowledges the support from S. Du and Y. Lyu. **Funding:** This study was supported by US National Science Foundation (NSF) (grant OISE-1743738, EAR-2103041, and AGS-2402113) to M.V. H.G. is funded by the Belgian Fonds de la Recherche Scientifique (F.R.S.-FNRS). V.F.N. was funded by the Deutsche Forschungsgemeinschaft (DFG, German Research Foundation) - project no. 395588486. F.W.C. was funded by Fundação de Amparo à Pesquisa do Estado de São Paulo (FAPESP) (grant 2017/50085-3) and Conselho Nacional de Desenvolvimento Científico e Tecnológico (CNPq) (grant 309755/2022-0). N.M.S. was funded by Fundação de Amparo à Pesquisa do Estado do Rio de Janeiro (FAPERJ) (grants E-26-201.421-2021 and E-26211.352-2021) and CNPq (grant 312343/2022-1). **Author contributions:** Conceptualization: Z.L. and M.V. Methodology: Z.L., M.V., and H.G. Investigation: Z.L., M.V., H.G., and R.O. Visualization: Z.L. Funding acquisition: M.V. Supervision: M.V. Writing—original draft: Z.L and M.V. Writing—review and editing: Z.L., M.V., H.G., R.O., V.F.N., F.W.C., J.C., and N.M.S. **Competing interests:** The authors declare that they have no competing interests. **Data and materials availability:** All data needed to evaluate the conclusions in the paper are present in the paper and/or the Supplementary Materials. The raw oxygen isotope data used in the DA reconstruction and independent local hydroclimate records are available from the SISAL database (https://researchdata.reading.ac.uk/256/), the PANGAEA database (https://pangaea.de/), and NOAA's National Climatic Data Center's Paleoclimatology database (http://ncdc.noaa.gov/paleo/paleo.html). Gridded observational and reanalysis datasets used in this study are available from ERA5 (https://cds.climate.copernicus.eu/cdsapp#!/dataset/reanalysis-era5-pressure-levels-monthly-means) and GPCC (www.psl.noaa.gov/data/gridded/data.gpcc.html). The simulation data from isotope-incorporated Global Spectral Model version 2 (IsoGSM2) are available at https://datadryad.org/stash/dataset/doi:10.6078/D1MM6B. Reconstructions of PWC and the Atlantic ITCZ are available from the following sources: Falster *et al.* (*36*): https://zenodo.org/records/10951789; Yan *et al.* (*35*): www.ncei.noaa.gov/metadata/geoportal/rest/metadata/item/noaa-recon-12203/html; Steinman *et al.* (*33*): www.datacommons.psu.edu/commonswizard/MetadataDisplay.aspx?Dataset=6340; and Haug *et al.* (*34*): www.ncei.noaa.gov/access/paleo-search/study/2560. Our DA reconstruction is available in Zenodo (https://doi.org/10.5281/zenodo.13145705).

Submitted 29 February 2024
Accepted 13 August 2024
Published 20 September 2024
10.1126/sciadv.ado9543